JACS
JOURNAL OF THE AMERICAN CHEMICAL SOCIETY
Article
pubs.acs.org/JACS

Structure and Stability of SnO_2 Nanocrystals and Surface-Bound Water Species

Hsiu-Wen Wang,*[,†] David J. Wesolowski,[†] Thomas E. Proffen,[‡] Lukas Vlcek,[†] Wei Wang,[§] Lawrence F. Allard,[∥] Alexander I. Kolesnikov,[‡] Mikhail Feygenson,[‡] Lawrence M. Anovitz,[†] and Rick L. Paul[⊥]

[†]Chemical Sciences Division, [‡]Chemical and Engineering Materials Division, [§]Environmental Sciences Division, and [∥]Materials Science and Technology Division, Oak Ridge National Laboratory, Oak Ridge, Tennessee 37831, United States

[⊥]Chemical Science Division, Materials Measurement Laboratory, National Institute of Standards and Technology, Gaithersburg, Maryland 20899, United States

Supporting Information

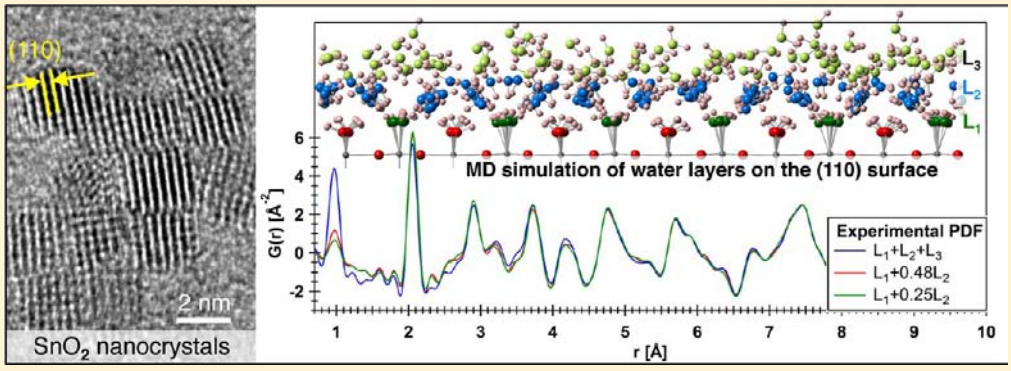

ABSTRACT: The structure of SnO_2 nanoparticles (avg. 5 nm) with a few layers of water on the surface has been elucidated by atomic pair distribution function (PDF) methods using in situ neutron total scattering data and molecular dynamics (MD) simulations. Analysis of PDF, neutron prompt gamma, and thermogravimetric data, coupled with MD-generated surface D_2O/OD configurations demonstrates that the minimum concentration of OD groups required to prevent rapid growth of nanoparticles during thermal dehydration corresponds to ~0.7 monolayer coverage. Surface hydration layers not only stabilize the SnO_2 nanoparticles but also induce particle-size-dependent structural modifications and are likely to promote interfacial reactions through hydrogen bonds between adjacent particles. Upon heating/dehydration under vacuum above 250 °C, nanoparticles start to grow with low activation energies, rapid increase of nanoparticle size, and a reduction in the *a* lattice dimension. This study underscores the value of neutron diffraction and prompt-gamma analysis, coupled with molecular modeling, in elucidating the influence of surface hydration on the structure and metastable persistence of oxide nanomaterials.

INTRODUCTION

Understanding the metastable persistence of engineered metal oxide nanoparticles and interactions with environmental matrices is critical to their synthesis and use. Cassiterite (SnO_2) and isostructural rutile (α-TiO_2) are naturally occurring minerals frequently used in pure form as solid-state gas sensing materials, oxidation catalysts, and transparent conductors.[1−4] Unlike α-TiO_2 gas sensors that can work at high temperatures mainly in combustion systems, SnO_2 is a typical low-temperature gas sensor. Above 400−500 °C, SnO_2 sensors (thin-film types) suffer from structural instability and poor selectivity.[5−12] Understanding the role of water in the stability and functional properties of SnO_2 nanosensors is critical. For instance, it has been reported that water adsorption facilitates the catalytic conversion of CO to CO_2 over SnO_2 catalysts[3] and that the formation of hydrated surfaces plays an essential role in stabilizing SnO_2 nanoparticles.[13] Among all the progress in characterizing the structure, dynamics, and speciation of the first few layers of sorbed water on SnO_2 at the dominant (110) crystal surfaces,[11,12,14−18] study of the interfacial water structure is a subject of long-standing interest, in relating the results of macroscopic measurements (e.g., surface energy,[3,13] enthalpy of adsorption,[13] and dissolution/growth rate[3]) to molecular scale processes (e.g., activity and ionic nature of surface sites,[3,7−10] and compact/diffuse model of the electrical double layer configuration[11,12,18]) under natural and laboratory conditions.

Coupled X-ray crystal truncation rod and molecular dynamics (MD) simulation studies[11] unambiguously identify at least two distinct layers of sorbed water for on the SnO_2 (110) single-crystal surface in contact with thick films (~2 μm) of bulk water, with O_w at heights of ~2.1 Å (denoted as L_1) and

Received: December 13, 2012
Published: April 22, 2013

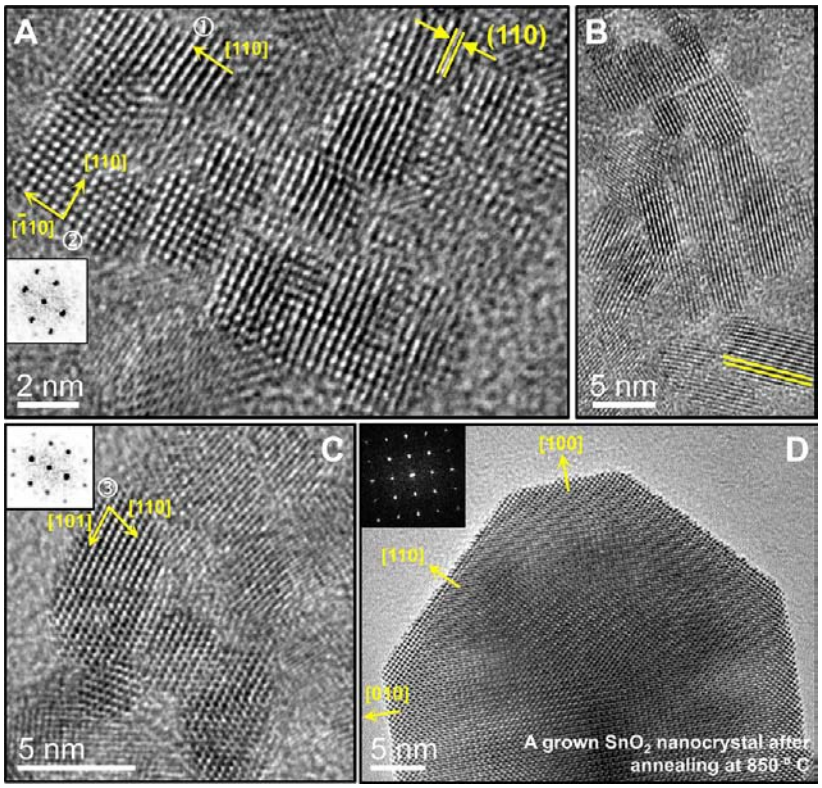

Figure 1. (A–C) HRTEM images of as-synthesized SnO_2 nanocrystals. The yellow parallel lines highlight the orientation between two parallel (110) facets. In the first coordinate, the [110] direction is indicated by a yellow arrow. In the second and third coordinates, the [001] and [111] are normal to the image, respectively. (D) HRTEM images of grown SnO_2 nanocrystals annealed at 850 °C. Inserts show FFT analyses of the second and third coordinates and grown SnO_2 crystals.

~3–4 Å (denoted as L_2) above the Sn–O surface plane. A third, less distinct layer (L_3) that exhibits a higher density than bulk water, is indicated at ~5–7 Å. MD simulations at reduced water coverage up to 4 monolayers (MLs)[11,18] suggest that this surface water structuring is not significantly altered in the absence of a bulk water phase. One ML on the (110) surface is defined here as the amount of water required to coordinate every bare Sn atom exposed on the vacuum terminated surface (equivalent to L_1), regardless of whether that water exists as intact water molecules at the "terminal" site directly atop each bare five-coordinated surface Sn atom or dissociated to form OH groups at the terminal Sn and adjacent "bridging" O sites.[11,18] Density functional theory (DFT) calculations for sorbed water on the SnO_2 (110) surface suggest that (partial) dissociative adsorption in L_1 is energetically favored.[3,12,14−17] At half-ML coverage, molecular adsorbed water was reported to be unstable on the SnO_2 (110) surface,[15] though the degree of dissociation of the L_1 water remains uncertain.[12,14−17] Recent DFT studies point toward a tendency for 60% dissociation in L_1,[17] though experimental studies have not unambiguously confirmed this conclusion. Gercher and Cox[7] performed thermal desorption spectroscopy and ultraviolet photoelectron spectroscopy for water adsorption on stoichiometric and reduced (defective) SnO_2 (110) surfaces. In their study, they found 15 ± 5% dissociated water on both surfaces, even though an increase in dissociation (up to 35 ± 5%; by a separate experiment) was observed on a less-defective surface.[7] The dependence of the amount of dissociation with surface O vacancies and defects is apparent.[7,9,10,19]

Measurements of water adsorption enthalpy showed that heat of adsorption for the chemisorbed water on the surface of SnO_2 nanoparticles is −75 kJ/mol-H_2O for 5 H_2O/nm^2 coverage.[13] The energy of water adsorption is higher (i.e., more negative by 31 kJ/mol-H_2O) than heat of adsorption for the physisorbed water, −44 kJ/mol-H_2O. The coverage of 5 H_2O/nm^2 corresponds to 1.1 H_2O per (110) Sn_2O_4 surface unit ($Å^2$) if the surface is assumed to be composed largely of this crystal face, which is close to the 1 ML coverage on SnO_2 (110). Corresponding measurements of drop solution enthalpy suggested that the anhydrous surface energy of SnO_2 is 1.72(1) J/m^2.[13] Heat capacity studies of surface water on SnO_2 nanoparticles indicated that "inner-type water" has a higher heat capacity than that of "outer-type water" for temperatures >200 K.[20] Shi et al.[20] attributed this curious thermodynamic result to the low surface energy of SnO_2, which yields stronger interactions between inner- and outer-type water than interactions between inner water to SnO_2 surfaces. Their arguments would suggest that water affinity for SnO_2 surfaces is weaker than the water phase itself, which is opposite to the aforementioned MD-DFT results. Note that the L_1–L_3 hydration layers in our MD model[11,18] differ from those described by Shi et al.,[20] where the terminology of "inner- vs outer-type water" used for interpreting heat capacity results is less specific. Furthermore, both L_1 and L_2 exhibit a high degree of vertical and lateral ordering in registry with the surface structure, and L_3 is recognized by its more weakly structured configuration and possesses faster water diffusional dynamics (from quasi-elastic neutron scattering, QENS, coupled with MD) as compared with L_1 and L_2.[18] In addition to QENS data, inelastic neutron scattering (INS) studies suggested that hydrogen-bond network for sorbed water molecules on SnO_2 is softer and more perturbed in the librational bands as

dx.doi.org/10.1021/ja312030e | J. Am. Chem. Soc. 2013, 135, 6885–6895

compared to the network within ice−Ih,[21,22] which is a suggestive of the extent of the water−SnO_2 interactions.

Validation of surface-bound water structure and the effect of sorbed water on the structure and metastability of SnO_2 nanocrystals are the focus of this contribution, in which we report new results from neutron total scattering data that reinforce our previous MD model[11,18] for the structural configuration of surface hydration layers on SnO_2 nanocrystals. There have been a number of studies characterizing structure,[4,23−26] size effects,[20,21,24,26,27] and growth mechanisms[4,26,28−32] of SnO_2 nanocrystals by ex situ X-ray diffraction (XRD), high-resolution transmission electron microscopy (HRTEM), and Raman scattering methods. The high atomic scattering factor of Sn relative to O for both X-rays and electrons influences the precise determination of lattice distortions and the structure of surface capping molecules as a function of nanoparticle size and hinders probing interfacial water−SnO_2 interactions. Neutron diffraction is not affected by such issues, since H and D atoms scatter neutrons as strongly as do Sn and O atoms. Coupling neutron total scattering with MD simulations provides powerful insights into the structure of hydration water on nanoparticle surfaces.

EXPERIMENTAL SECTION

SnO_2 Nanoparticle Synthesis and Basic Characterization. SnO_2 nanocrystals synthesized through solution-phase growth are described in Mamontov et al.[18] Synthesis, purification (by dialysis), and capping of SnO_2 surfaces by water molecules were conducted entirely in either H_2O or D_2O water. SnO_2 nanopowders with protiated or deuterated surfaces are used for different types of neutron experiments. The very large incoherent scattering cross section of H is ideal for QENS[18] and INS studies of diffusional and vibrational dynamics (manuscript in preparation). For the elastic scattering studies of structure reported here, deuterated samples are needed to minimize the incoherent background contribution from H atoms. For both syntheses, morphologies of as-synthesized nanocrystals were first investigated using cold-field emission TEM (Hitachi HF3300, operated at 300 kV). As shown in Figure 1A−C, SnO_2 nanocrystals have rod- to cube-like or more rounded habits with particle size ∼3−6 nm. HRTEM images also reveal that (110) faces are the likely dominant surface terminations, satisfying the theoretical prediction that the (110) surface has the lowest surface energy followed by the (100), (010) < (101) < (201) < (001) surfaces.[3] Note that the (110) crystal faces do not constitute a closed form, and other terminations of the nanoparticles must also be present (see Figure 1 and Section 1 in Supporting Information (SI) for more HRTEM images). The specific surface area of 153(1) m^2/g determined using N_2 Brunauer−Emmet−Teller (BET, Micrometrics Gemini VII2390) method yields an average particle size of 5.6(1) nm (assuming perfect spheres), consistent with HRTEM observations. Thermogravimetric (TG) analysis (∼20 mg of sample; 10 °C/min heating rate with a 70 cm^3/min air flow through the system) of protiated SnO_2 nanocrystals before and after purification is shown in Figure 2 (the left axis). The unpurified sample was prepared via simply rinsing clean with H_2O or D_2O water, whereas the purified sample was prepared by an additional dialysis procedure. All neutron data were collected from the purified samples. The TG weight loss and the temperature derivative of the TG curve observed in the unpurified sample (green lines in Figure 2) emphasize the importance of the cleaning process, because additional amounts of the weight loss are contributed by chlorine (Cl), presumably as residual chloride from the synthesis (discussed below). Preparation of purified SnO_2 nanocrystals with three different surface water contents, referred to as the "full", "half", and "dry" samples, is described in Section 2 of SI. TG curve for the full sample (i.e., full hydration) is shown in Figure 2. The dry sample is purified nanopowders with the least amount of sorbed water that can be achieved during preparation (i.e., the driest achievable state under rough vacuum conditions of

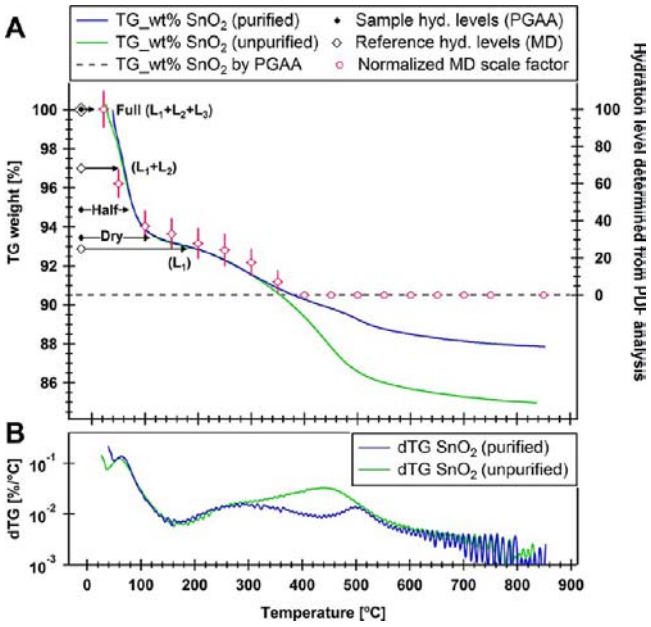

Figure 2. (A) Left axis: TG analysis of purified (blue line) and unpurified (green line) SnO_2 nanopowders. The black dashed line marks the total amounts of sorbed water species (9.49 wt %, determined by PGAA) in the fully hydrated sample. The black diamond symbols represent sorbed water contents (by PGAA) in the three prepared samples, and the white diamond symbols represent reference hydration levels calculated based on MD. Right axis: Hydration level determined from PDF analysis, which is based on normalized scale factor (pink circles with error bars) of MD hydration phase fitted at each temperature. The left and right axes are adjusted in the same scale for an easy comparison. (B) The temperature derivative of the TG weight loss curve (plotted in a logarithm scale) for purified and unpurified samples.

∼0.02 bar at 180 °C for 8 h). In this communication, TG analysis and neutron prompt-gamma activation analysis (PGAA) of total H were performed on the protiated samples, whereas neutron total scattering and atomic pair distribution (PDF) analysis were conducted on the deuterated samples.

Neutron PGAA. The neutron-induced PGAA of the H_2O/OH capped powders was conducted in the beamline NG-7 at the Center for Neutron Research, National Institute of Standards and Technology, as described by Paul and Lindstrom.[33] About 1 g of each purified sample (full, half, and dry) was loaded and sealed with an indium O-ring in the flat aluminum sample holder (25 × 25 × 0.5 mm^3) and mounted directly in the beam, measuring the γ-rays emitted by each constituent element. Neutrons penetrate the samples uniformly, so the contents of Sn, H, residual Cl, and possibly nitrogen contaminations in the three samples are precisely quantified by PGAA. The mole ratio for H and Cl relative to Sn is determined by comparing areas of peaks in the spectrum of the sample to corresponding peaks in the spectrum of a standard (cf. Anderson et al.)[34] containing a known quantity of the elements. Results are summarized in Table 1, and spectra of a characteristic prompt γ-ray for H (2223.23 keV) in the three samples are shown in Figure 3A. No nitrogen was detected in any samples.

Neutron Total Scattering. Data were collected on the NOMAD beamline at the Spallation Neutron Source, Oak Ridge National Laboratory, as described by Neuefeind et al.[35] The purified full, half, and dry samples (∼2 g each) capped with D_2O/OD species were tightly packed in vanadium sample cans (6 mm diameter) with a Cu-seal gasket and a control valve to regulate the atmosphere over the sample. Micron-sized SnO_2 bulk powder and the three prepared/sealed nanopowder samples were first measured for 1 h at room temperature (∼22 °C). The observed intensities were normalized by

dx.doi.org/10.1021/ja312030e | J. Am. Chem. Soc. 2013, 135, 6885−6895

Table 1. Water Content Details for the Full, Half, and Dry SnO_2 Samples

	PGAA[a]			no. H_2O/OH[b]		PDF	formula	MD model[c]
samples	H/Sn ; Cl/Sn mole ratio	H_2O ; Cl wt %	normalized H/Sn ratio[d]	per nm^2	per unit (110) Sn_2O_4 surface ($Å^2$)	norm. Gaussian peak area of 0.98(3) Å	$SnO_2 \cdot xH_2O$ (by PGAA)	no. of hydration layers
full	1.786; 0.077	9.49; 1.61	1.000	20.74	4.43	1.000	0.877	$L_1 + L_2 + L_3$
half	0.775; 0.077	4.35; 1.70	0.434	9.50	2.02	0.453	0.380	$L_1 + 0.48L_2$
dry	0.601; 0.077	3.41; 1.71	0.336	7.44	1.59	0.343	0.295	$L_1 + 0.25L_2$

[a]Expanded uncertainties on values measured by PGAA are estimated at 5−10%. [b]Number of H_2O/OH molecules per area is calculated based on PGAA and BET results. [c]Average number of H_2O/OH molecules per hydration layer is $L_1 = 1.00$, $L_2 = 1.73$, and $L_3 = 1.27$ for a total of 4 D_2O/OD molecules per (110) Sn_2O_4 surface unit. See Mamontov et al.[18] for further details. [d]Normalized H/Sn ratio is calculated based on the fully hydrated sample, i.e., the full sample has a ratio of 1, the half sample has a ratio of 0.775/1.786, and the dry sample has a ratio of 0.601/1.786.

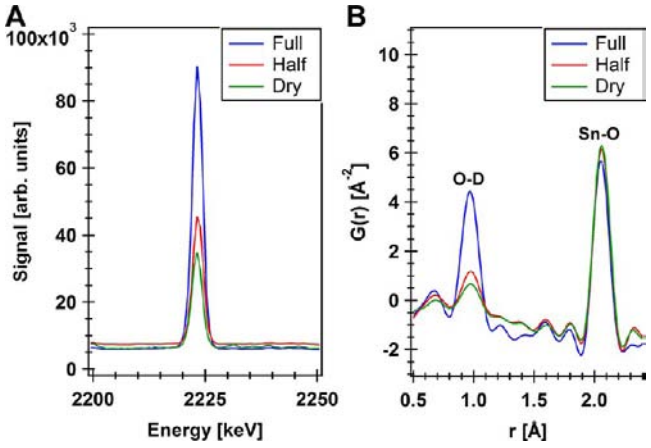

Figure 3. (A) PGAA spectra of H in the full, half, and dry samples. The H signal is scaled relative to the full sample according to the measured Sn signal. (B) Observed PDFs of the O−D bond distances in the three prepared samples. For both results, the peak area is proportional to the amounts of water species presented on the nanoparticles surfaces.

scattering from a vanadium rod, and background scattering from the empty container was subtracted. The experimental PDF was obtained by a Fourier transform of the total scattering structure function $S(Q)$ up to Q_{max} of 31.5 $Å^{-1}$. In situ thermal dehydration experiments were performed on the fully hydrated sample under the detector vacuum conditions (~10^{-7} bar) with the control valve open to vacuum (to prevent overpressure in the sample holder upon dehydration). Sample temperature was controlled via Institut Laue-Langevin furnace, which provides the opportunity for measuring scattering data as a function of temperature at ~22 °C, then from 50 to 750 °C in 50 °C increments, and at 850 °C as the highest temperature point. We used 3.33 °C/min heating rate and allowed 15 min waiting time before data collection (1 h for each set temperature). The 15 min equilibrium time was judged from the isothermal growth experiments done by Lai et al.,[28] in which they showed that the grain size of SnO_2 nanoparticles increased rapidly at the first 20 min of annealing time and then reached a limiting size for a given annealing temperature. At each set-point temperature, the first and last 10 min data were compared to ensure no significant grain growth occurred within the 1 h collection time. All experimental PDFs were analyzed using the software package PDFgui.[36] Instrument resolution parameters, $Q_{damp} = 0.0219(2)$ and $Q_{broad} = 0.0239(3)$, were determined with Ni bulk powder (99.99%, Sigma Aldrich) measured under similar conditions.

RESULTS

Water Content: Comparing TG Analysis with PGAA and PDF Results. As seen in Figure 2A (blue line), the total amount of weight loss for the purified fully hydrated sample based on TG analysis is 12.14 wt %, with a sharp TG dehydration curve at temperatures <100 °C followed by a gradual weight loss up to ~380 °C. The temperature derivative of the TG curve is characterized by two peaks centered at ~50 and ~270 °C, respectively, suggesting the loss of surface-bound water species. At temperatures >380 °C, different amounts of weight loss are observed in TG data for the purified (blue lines) and unpurified (green lines) samples. Additional weight loss in the unpurified SnO_2 was likely contributed from loss of residual Cl, and this is best seen in the temperature derivative of the TG curve, which shows an additional peak centered at ~440 °C as compared with the purified sample data. On further heating, both samples show a continuous weight loss up to 850 °C, and there is a clear derivative peak (at ~500 °C) in the purified sample which perhaps indicates the loss of surface O from SnO_2 nanoparticles at high temperatures. Batzill and Diebold[3] reviewed the evolution of SnO_2 (110) and (100) surfaces with increasing sample temperature under ultrahigh vacuum (UHV) conditions for initially fully oxidized surfaces. They reported that a fast depletion of O from (110) and (100) surfaces occurred in a temperature range of 170−250 and 340−390 °C, respectively. Since our TG data were obtained in the constant airflow conditions, the O loss from nanoparticle surfaces likely occurred after removal of surface-bound species and at relatively higher temperatures in an O_2-rich atmosphere than under UHV conditions.

Absolute water contents in the purified full, half, and dry samples were determined from H/Sn mole ratio based on PGAA measurements and are given in Table 1. The full sample contains only 9.49 wt % of water, which corresponded to the TG weight loss observed at temperatures <380 °C, as indicated by the black dashed line in Figure 2A. The additional 2.65% TG weight loss is mainly contributed from residual Cl (1.61 wt %; based on PGAA) and surface O from the sample (1.04 wt %; based on total weight loss, i.e., 1.04 wt % = 12.14 − 9.49 − 1.61 wt %). Absolute water contents in the half (4.35 wt %) and dry (3.41 wt %) samples obtained based on PGAA H/Sn mole ratio are also marked by black diamond symbols in Figure 2A. Furthermore, according to PGAA and BET surface area results, the number of H_2O/OH molecules per surface area and per (110) Sn_2O_4 surface structural unit can be determined. As summarized in Table 1, coverage of 4.43, 2.02, and 1.59 of H_2O/OH per (110) Sn_2O_4 surface unit for the full, half, and dry samples, respectively, were obtained with the assumptions that the surface is composed largely of (110) crystal faces. The relative values of surface water coverage in the three samples can also be extracted from the area under the peak (fitted with a Gaussian) at the O−D distance of 0.98(3) Å in the PDF data (Figure 3B). As shown in Figure 3 and Table 1, the PGAA spectra are consistent with the normalized areas of the O−D distance peak in the PDF results. See Section 3 of SI for further discussion.

MD Simulations and Models of Water−SnO_2 Interface. The amount of sorbed water required to mimic the hydration level in the experimental nanoparticles was calculated based on the assumption that only the (110) surface is exposed, which is a simplified interfacial model for a nanoparticle system. This fact should be borne in mind because the simulation did not consider other surface terminations, defects, and effects of nanoparticle shapes to the disruption of layered hydration structure. This simplified model, however, provides a starting point for data-driven modeling of the experimental PDF data, which begins with least-squares like modeling of the separate phases (e.g., SnO_2 substrate and sorbed water layer) and ultimately moves to multilevel general minimization modeling schemes[37] for a complete water−SnO_2 interfacial structure. In this study, only a two-phase modeling scheme is presented, considering the nanoparticles as monolithic single crystals as one phase and the MD-generated (110) surface water structure as the other phase.

Water coverage determined by PGAA agrees well with our previous MD studies[18] with 4.0 H_2O/OH molecules per (110) Sn_2O_4 surface unit, corresponding closely to our fully hydrated sample. Here we repeated the simulations with a slightly modified water model, SPC-HW,[38] taking into account small differences in water−SnO_2 interactions between H_2O/OH and D_2O/OD. The coverage of 4.0 water molecules per (110) Sn_2O_4 surface unit results in the formation of three structurally distinct hydration layers (L_1, L_2, and L_3), as discussed above. We simulated two forms of the hydrated (110) surface: nonhydroxylated, representing molecularly adsorbed L_1 D_2O on five-coordinated Sn sites, and hydroxylated, representing fully dissociated D_2O molecules (i.e., terminal and bridging OD species) in the L_1 layer. The two surface forms with OD hydroxyls and adsorbed D_2O molecules are illustrated in Figure 4. The MD simulation box size was 38 × 41 × 60 Å^3, with two

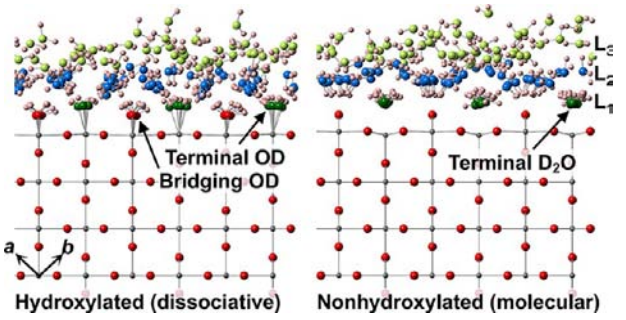

Figure 4. MD snapshots of hydroxylated (dissociative adsorption) and nonhydroxylated (molecular adsorption) configurations on SnO_2 (110) surfaces. Sn atoms, gray spheres; O atoms, red spheres; O atoms in L_1 species, dark-green spheres; O atoms in L_2 species, blue spheres; O atoms in L_3 species, light-green spheres; H atoms, light-pink spheres; and bonds, solid gray lines.

parallel SnO_2 blocks separated by 41 Å in the z-direction. Each block exposed 72 (110) surface Sn_2O_4 units to the interior of the slit pore, which was filled with the appropriate amounts of D_2O to achieve the desired hydration level. Note that water molecules only very rarely escape the surface hydration layers during the simulation and quickly readsorb or migrate and readsorb on the other side of the gap. The amounts of D_2O are given in Table 1 in terms of fractions for each hydration layer. Further MD simulation details are presented in our earlier works.[11,18]

Structure of Surface-Bound Water Analyzed by PDF and Real-Space Refinements. Figure 5A shows the experimental PDFs for the full, half, and dry SnO_2 nanopowder samples and micrometer-sized SnO_2 (bulk) crystallite powders obtained by gently crushing SnO_2 single crystal filaments grown via chemical vapor-deposition.[11] The presence of sorbed water species on nanoparticles is clearly seen, and the PDF signals of the nanopowders were damped at r > ∼40 Å, suggesting disappearance of long-range order due to the limits of particle size. In SnO_2 bulk crystallites, because of the long-range order of the structure, all neighbors and all lengths are well-defined which gives rise to sharp PDF peaks as compared with nanocrystals. Signals from contaminates, such as H−Cl and Sn−Cl pairs, at distances of ∼1.27 and 2.36 Å (Shannon ionic radii)[39] cannot be observed, and hence we do not consider the presence of Cl in the modeling. Figure 5B shows the calculated PDFs of hydration layers on the (110) surface at the hydration levels of the full, half, and dry samples, using the non-hydroxylated and hydroxylated MD models. As seen in Figure 5B, the peak intensity at 0.98(3) Å is proportional to the hydration level in the system, the 1.63(3) Å peak is the D−D distance of the D_2O molecule, and a weak intensity lying on the high-r shoulder of the 1.63(3) Å peak is from the intermolecular O−D distances between nearby water molecules. The broad PDF signal in the r-range of 2−5 Å originates from longer range water−water correlations within and between layers. At r > 5 Å, a much weaker PDF signal is observed, and this is likely due to the lack of lateral-ordering parallel to SnO_2 surfaces for the outermost hydration layer (L_3) as compared with the first two layers (L_1 and L_2). The differences between nonhydroxylated and hydroxylated configurations are clearly seen when only the L_1 species is present, indicated by the presence of the D−D peak in the nonhydroxylated configuration only. For higher hydration coverage, these two models give similar results in both low- and high-r ranges, because all intact D_2O molecules have similar O−D and D−D distances and the outer hydration layers (L_3 and part of L_2) do not possess significant differences in lateral ordering.

To further interpret PDF data, a trial fit was first applied to the hydrated nanopowder, using a two-phase model, the SnO_2 bulk structure + "dummy OD pair", designed to account for O−D peak observed at 0.98(3) Å and nanoparticle structure observed at r > 2 Å. Structural parameters for SnO_2 were obtained from Bolzan et al.[40] as a starting point in PDF refinements. During the fit we varied the overall intensity scale factor, the unit cell, the x-coordinate of O, and the thermal displacement (U_{ij}) for both Sn and O in SnO_2 phase (all constrained by the $P4_2/mnm$ space group). The r dependence of the SnO_2 PDF peak width due to correlated thermal motions was refined using the variable delta1 (δ_1). A spherical envelope function, involving the shape damping parameter (spdiameter), was also included in order to model the finite particle size effect. The phase of "dummy OD pair" is a 4 Å cubic box with an OD group sitting at each corner as a primitive cell. During the fit a proper cutoff value (stepcut = 1.9 Å) was kept fixed to avoid periodic boundaries for "dummy OD pair" phase, and only the scale factor, the cubic unit cell and the isotropic U_{ij} for D and O were varied. The fit r range was 0.7−50 Å, and Q_{damp}, Q_{broad}, and Q_{max} values were fixed during the refinements. After several refinement cycles, a suitable fit was obtained, and results for the fully hydrated sample are shown in Figure 5C (reports for the final refined parameters for the full, half, and dry

dx.doi.org/10.1021/ja312030e | J. Am. Chem. Soc. 2013, 135, 6885−6895

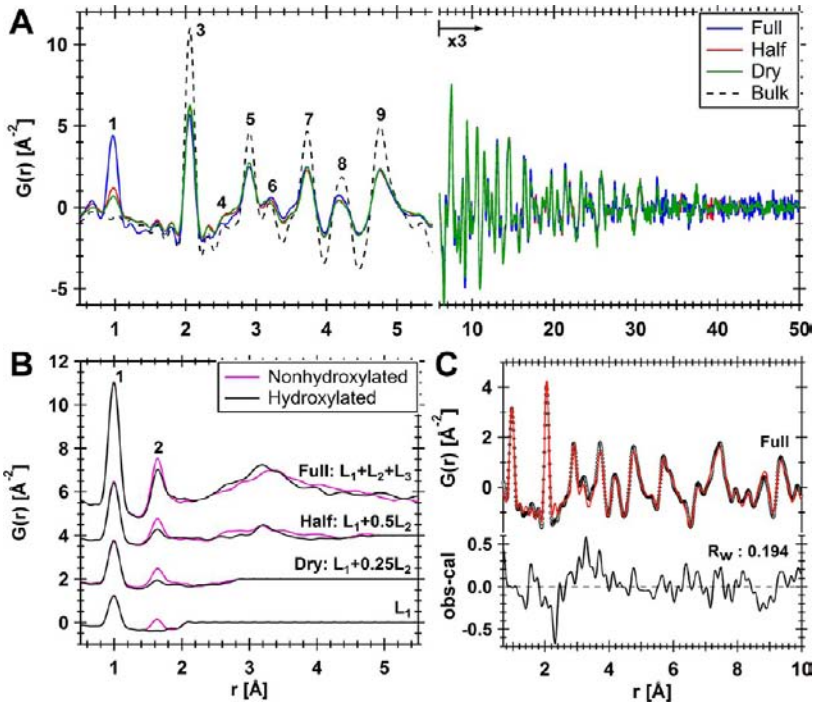

Figure 5. (A) Observed PDFs of the full, half, and dry samples and their comparisons with bulk SnO_2. For clarity, the PDF result of SnO_2 bulk powder at $r > 6$ Å is not shown. (B) Calculated PDFs of surface hydration layers from two different MD models. Peak label 1 = O−D; 2 = D−D; 3 = Sn−O; 4/5 = first coordination shell of O−O; 6 = first coordination shell of O−O and Sn−Sn (*c* axis); 7/8 = second coordination shell of Sn−Sn, Sn−O, and O−O; and 9 = second coordination shell of Sn−Sn (*a* axis). (C) PDF fit of the fully hydrated sample using a two-phase model (SnO_2 bulk structure + "dummy OD pair"). The black circle and the red curve show the observed and calculated PDFs, respectively. The black curve at the bottom shows the difference between the two. Note that the PDFs and the difference curve are plotted on a different *y*-scale.

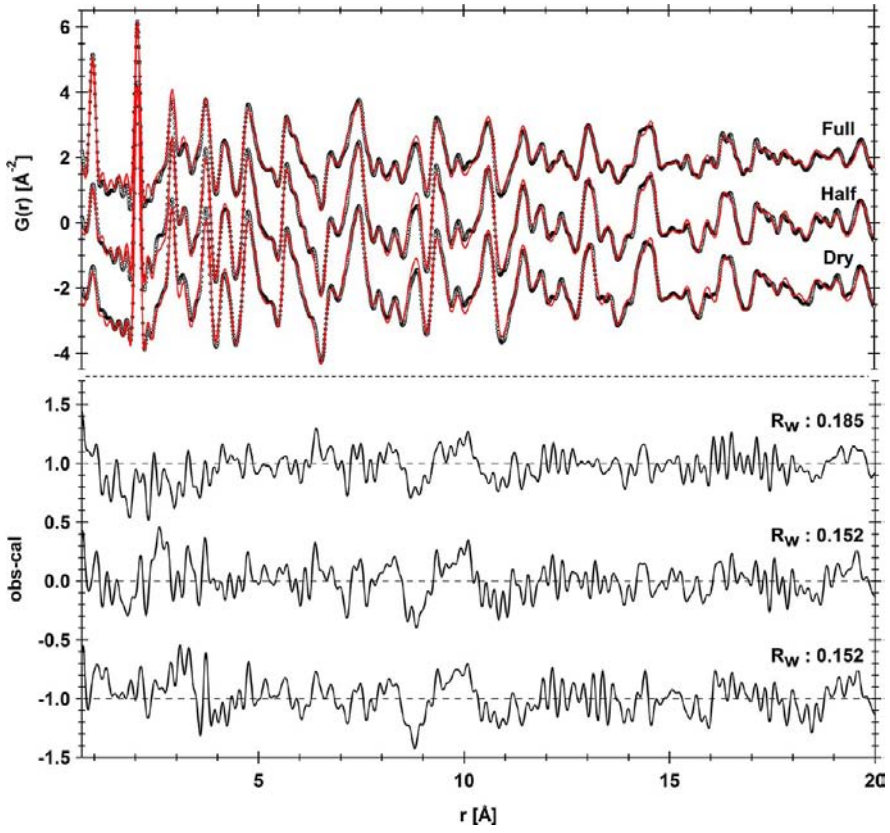

Figure 6. PDF fits of the full, half, and dry samples using a two-phase model (SnO_2 bulk + the hydroxylated MD structures). Results are stacked by offset of a constant *y*-intensity. Curves and symbols are the same as in Figure 5C.

dx.doi.org/10.1021/ja312030e | *J. Am. Chem. Soc.* 2013, 135, 6885−6895

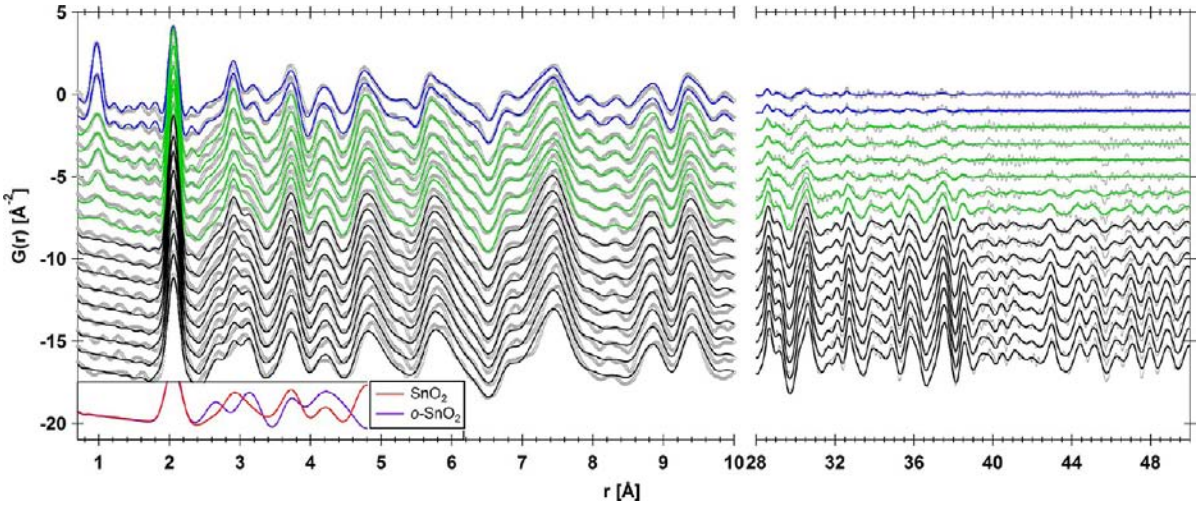

Figure 7. Temperature-resolved PDFs plotted in order of increasing temperature, in a sequence of (1) blue curves = ~22, 50 °C; (2) green curves = 100, 150, 200, 250, 300, 350 °C; and (3) black curves = 400, 450, 500, 550, 600, 650, 700, 750, 850 °C. The gray circle shows the observed PDFs obtained through Fourier transformation of the $S(Q)$ data given in Figure S3 in SI. The calculated PDFs are shown by the blue, green, and black curves. The insert graph illustrates the calculated PDFs between *o*-SnO_2 and SnO_2 structures at r < 5 Å.

samples are given in Section 4 of SI). The refined particle size for all three samples is 46(3) Å, which is similar to HRTEM and BET observations and also suggests that our drying treatments have not yet caused any significant size changes in nanoparticles. Significant residual error is observed from the difference plot in the r = 2−5 Å region (Figure 5C).

To fit observed PDFs with the MD-derived hydration structure and to extract the phase fractions of sorbed water species, a two-phase model fit, combining SnO_2 bulk and the hydroxylated MD structures, was applied (the use of hydroxylated MD model instead of nonhydroxylated one is further explained below). In order to reduce the number of variables, all the D_2O/OD coordinates in the hydration layer phase were kept unchanged, and large isotropic U_{ij} for D and O were applied and fixed at 0.02 Å^2 during the fit. The sharpening parameter (sratio), allowing sharpening of the PDF peaks below a given r, was included in the MD hydration phase in order to sharpen the O−D peak observed at r < 1 Å. The combination of large U_{ij} and sharpening parameter for the MD hydration phase was found to be an effective strategy compensating the narrow and relatively broad distribution of O−D and D-D distances, respectively. Furthermore, to fit PDFs of the three samples, proper stepcut value and hydration coverage were also considered. For the fully hydrated sample, a use of L_1 + L_2 + L_3 coverage and 5 Å stepcut value were applied. For the half-hydrated sample, a use of L_1 + L_2 coverage and 4 Å stepcut value were applied. For the dry sample, only L_1 species and 2 Å stepcut value were used during the fit. Only the scale factor, the sratio value, and the box size were refined in the MD hydration phase. All the other variables, including those used in SnO_2 phase, are the same as those in the "dummy model" fitting. Final fits for the three samples are shown in Figure 6, and reports for the refined parameters are tabulated in Section 4 of SI. Improvements of the fit for longer water−water correlations at r range of 2−5 Å are observed. However, the rigid water model used in MD seems to overestimate the D−D pair distributions in the full sample, even though a large value of U_{ij} was applied. Interestingly, the fit for the dry sample is good at r < 2 Å, and all the Fourier termination ripples are fitted with no obvious mismatches between the observed and modeled PDFs, which indicate that the use of the hydroxylated configuration does give a good fitted result. On the other hand, as can be observed from Figure 5B, the nonhydroxylated configuration will result in overestimation of intensity in the D−D pair region, especially for the dry and perhaps half samples.

Evolution of SnO_2 Nanocrystals upon Dehydration. Temperature-resolved PDFs from in situ dehydration experiments demonstrate the growth of SnO_2 nanoparticles upon dehydration. As seen in Figure 7, above 250 °C, SnO_2 nanocrystals started to grow as noted by the increase of PDF signals at r > 28 Å. By 400 °C, strong PDF signals (at r > 28 Å) of the SnO_2 continue to develop, and observations of local structural distortions in the r-range between 2.4 and 3.4 Å are clearly seen. This suggests that the distortions are originating from local O−O distance variations, yielding distorted Sn octahedral geometries (see Section 5 of SI for temperature-resolved $S(Q)$ data).

To fit temperature-resolved PDFs, a two-phase model was applied, using a combination of SnO_2 bulk and the hydroxylated MD hydration structures as described above. The hydration coverage of L_1 + L_2 + L_3 was used for data measured at room temperature and 50 °C. A coverage of L_1 + L_2 was applied for data at 100, 150, and 200 °C. A coverage of L_1 only was applied for data at 250, 300, and 350 °C. No hydration phase was used for fitting data measured at 400−850 °C, but an orthorhombic modification of the SnO_2 bulk phase was introduced to account for local structural distortions observed at the low-r region (r < 5 Å), i.e., the high-temperature data were modeled with the coexistence of two different polymorphs of SnO_2 (the bulk tetragonal and an orthorhombic modification). The orthorhombic phase (referred to as *o*-SnO_2) has *Pnnm* symmetry (a subgroup of $P4_2/mnm$), which allows more distortions in the Sn octahedra via varying the a and b cell parameters and x- and y-coordinates of O. The *Pnnm* orthorhombic symmetry has been reported to exist in the high-pressure SnO_2 polymorph transformed directly from bulk phase at pressures in excess of 4.7 GPa under nonhydrostatic conditions at ambient temperatures.[41] However, attempts to index the 850 °C $S(Q)$ data (see Section 5 in

dx.doi.org/10.1021/ja312030e | J. Am. Chem. Soc. 2013, 135, 6885−6895

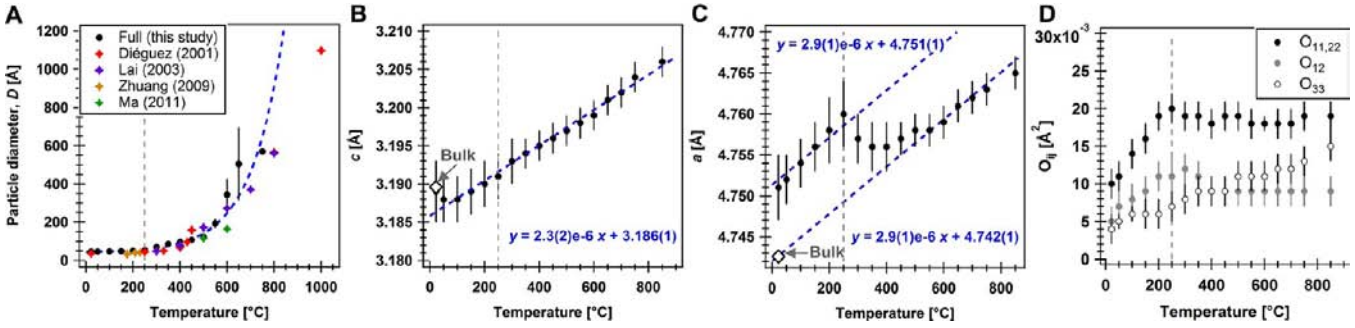

Figure 8. Changes in (A) SnO_2 nanoparticle sizes, (B) the *c* lattice dimension, (C) the *a* lattice dimension, and (D) U_{ij} for O as a function of temperature. The blue dashed lines in (A–C) show the regressions of the measured data. Particle (crystallite domain) size for the data point at 750 °C in (A) is obtained from Rietveld refinements using XRD data (see Section 8 of SI). The white diamond symbols in (B) and (C) are the unit-cell dimensions for SnO_2 bulk determined at ~22 °C. The vertical dashed lines in all plots mark changes observed below and above 250 °C. Expanded uncertainties for refined structural parameters are shown by error bars.

SI) with the high-pressure *Pnnm* polymorph reported in the literature[41−43] were unsuccessful, mainly due to not enough splitting between the *a* and *b* cell parameters as reported in the high-pressure structure. Allowing somewhat larger variations in both *a* and *b* cell parameters, a better indexing solution was obtained for *o*-SnO_2 phase (use of 850 °C data). The structure of *o*-SnO_2 determined at 850 °C [a = 4.16(1) Å, b = 5.24(1) Å, c = 3.16(1) Å, O(x, y) = 0.349(5), 0.271(5)] was used for PDF refinements at 250−850 °C in a simple manner with few parameters varied. The U_{ij} for Sn and O in *o*-SnO_2 phase were constrained to be the same as those in SnO_2 phase, and the only independent variable during the fit is the scale factor for *o*-SnO_2 phase. Comparison of calculated PDFs between *o*-SnO_2 and SnO_2 structures in a short-*r* range is illustrated as an insert graph in Figure 7. A summary table from PDF refinements is given in Section 4 of SI. SnO_2 nanocrystals annealed at 850 °C have grown into bulk-like crystallites with smooth euhedral crystal surfaces and distinct face angles (Figure 1D; see Section 6 of SI for HRTEM images of postexperiment annealed materials).

■ DISCUSSION

Summarizing the results discussed above, formation of hydration layers on SnO_2 surfaces reduces the surface energy of nanoparticles[13] and inhibits particle growth. Removal of these capped water species below a certain threshold allows the nanoparticle structure to transition to the bulk structure, leading to growth, as observed during thermal dehydration. Variations in surface water contents as a function of temperature determined from PDF analysis are presented in Figure 2. The right axis of Figure 2A represents changes of surface water contents derived from the scale factor (phase weight) of surface hydration phase, illustrating a good agreement between TG data (blue line) and neutron scattering results (based on temperature-resolved PDF fits; pink circles). Although results from dynamic TG measurements should be qualitatively comparable with static neutron total scattering measurements, they cannot be expected to be entirely equivalent, because the temperature ramp rate, amounts of sample used, and sample environments are quite different between these two experiments. Above 350 °C the O−D PDF signal disappears, indicating a complete removal of sorbed D_2O/OD species. This result is also consistent with total water contents (marked by black dashed lines in Figure 2A) determined by PGAA. It is important to note that results from PGAA and total scattering experiments (Figure 3) not only agree with the TG data but also confirm that not all the TG weight loss comes from sorbed water species. The hydroxylated MD model further suggests that the loss of L_1 (and part of L_2) species is likely associated with the TG weight loss observed at temperatures between 180 and 380 °C and the temperature derivative peak centered at ~270 °C (Figure 2).

Changes in the size of nanoparticles as a function of temperature are illustrated in Figure 8A, along with other published results. At 250 °C, L_1 species are being removed, at which point nanoparticles started to grow. This indicates that the minimum threshold of surface-bound water required to stabilize the nanoparticles based on 300 °C PDF data is ~0.7 ML coverage. In addition, as seen in Figure 8B−D which showed changes of structural parameters with temperature, observation of a second-order behavior involving a contraction of the *a* axis and variations in U_{ij} for O at temperatures >250 °C suggests that changes in SnO_2 structural behavior is primarily associated with grain growth. Thermal expansion (illustrated by blue dashed lines in Figure 8B,C) of the SnO_2 crystallite explains the linear increase of the *c* and *a* lattice dimensions with increasing temperature. However, unlike the *c* axis, the *a* axis exhibits a distinct step (begins at ~250 °C) to a more contracted bulk-like dimension, which is coincident with simultaneous changes in U_{ij} for O (Figure 8D), the start of rapid nanoparticle growth (Figure 8A), and the decrease of hydration coverage below ~0.7 ML. The slope (in nature logarithm) of blue dashed lines shown in Figure 8B,C is used to obtain the thermal expansion coefficients parallel ($\alpha_{\parallel}$) and normal ($\alpha_{\perp}$) to the *c* axis. The determined values for $\alpha_{\parallel}$ and $\alpha_{\perp}$ are 5.6(5) × 10^{-6} and 6.1(4) × 10^{-6} K^{-1}, respectively. Both values and the deduced volume expansion coefficient (α_v = $2\alpha_{\perp}+\alpha_{\parallel}$ = 17.8(5) × 10^{-6} K^{-1}) are in general larger than those reported for SnO_2 bulk crystals, which is between 3.7 × 10^{-6} and 5.3 × 10^{-6} K^{-1} for linear expansions either normal or parallel to the *c* axis.[44,45] Our determined values are, however, close to the α_v value of 17(7) × 10^{-6} K^{-1} obtained for the high-pressure cubic SnO_2 phase at 25 GPa.[46]

SnO_2 structural changes upon dehydration and grain growth presented in Figure 8 provide further insights into the properties of SnO_2 nanocrystals. Observation of the larger *a* unit-cell dimension as compared with SnO_2 bulk crystallites at room temperature (Figure 8C) indicates the particle-size-dependent structural modifications. Neutron PDF analysis reveals relatively larger lattice expansions than those

dx.doi.org/10.1021/ja312030e | J. Am. Chem. Soc. 2013, 135, 6885−6895

determined from synchrotron X-ray experiments (see Section 7 in SI). Our observations are, however, different from those concluded (based on synchrotron X-ray PDF) by Jensen et al.[26] in which they proposed that the *c* unit-cell dimension expands for small particle size,s whereas the *a* dimension is found to be independent of particle size. The different elemental sensitivities between neutron and X-ray scattering suggest that the origin of the lattice size dependency is primarily contributed from the positions of O atoms, yielding significant distortions around the Sn, especially near the surfaces (recalling the fact that scattering of X-rays from the heavy Sn atoms swamps out the subtle changes in structural positions of lighter elements O, D, and H). Expansion of the bulk unit cell at reduced crystallite sizes is well-known for several metal oxide systems (e.g., MgO,[47] CeO_2,[48] and α-TiO_2[49]), and different explanations have been given, such as valence reduction in the case of CeO_2 and surface defect dipoles in the case of α-TiO_2. It has been argued that the lattice expansion of α-TiO_2 at finite sizes is unrelated to valence changes of Ti with size, and instead the presence of dangling bonds, surface disorders, and molecular adsorptions at the surfaces induces surface dipole−dipole interactions, resulting in negative pressures and repulsive dipole forces responsible for a lattice expansion.[49] Accordingly, water adsorption on the (110) SnO_2 crystal surfaces can then explain why only the *a* lattice is expanded but not the *c* lattice, i.e., lattice expansion is primarily due to induced dipole repulsions dominant in the *ab* plane by sorbed water species. If the observed unit-cell expansion is truly due to surface defect dipoles induced by water adsorption, upon removal of sorbed water species, surface stress effects arising from surface curvatures at finite sizes should result in a net positive pressure and cell contractions along the *a* direction. Observation of a sudden contraction in the *a* lattice at temperatures between 250 and 500 °C appear to support the above explanations in which the formation of hydration layers on the (110) surfaces may play major roles in the observed lattice expansion and the nonlinear thermal expansion behaviors along the *a* axis. It is in fact quite possible that previous structural studies on such nanomaterials were not conducted in a way as to identify and quantify the role of water sorbed from normal laboratory, experimental, or synthesis environments, which may lead to interpretations that do not capture the role of water as a ubiquitous capping agent that influences both the structure and the metastable persistence of nanomaterials. As shown in Figure 8C, the biggest lattice contraction occurs at 300−350 °C, at which the surface water coverage is < ~0.7 ML coverage. By 400 °C, nanoparticle sizes already increased significantly, and thermal expansion along the *a* axis gradually approaches to the regular temperature extrapolation of the bulk-like behavior.

Even though we applied an orthorhombic modification of the *Pnnm* structure (i.e., *o*-SnO_2) to model the high-temperature PDF data (≥400 °C), the *o*-SnO_2 structure in the current modeling scheme does not imply any specific surface disorders and/or defect types formed during the growth. The observation of local structural distortions, however, suggests that the compressive stresses produced upon the growth of SnO_2 nanoparticles cause the Sn−O octahedral distortions, which may further explain why the metastable orthorhombic SnO_2 structure (in the *Pnnm* or *Pbcn* symmetries) is widely found to coexist with the regular cassiterite structure during the synthesis of SnO_2 thin films and nanowires.[3,4,23,50,51] Detailed analysis for surface defects and the origin of the unit-cell size dependency on various terminated surfaces using a single-phase model of water-SnO_2 interface (e.g., core−shell model) is needed to further support the above observations but is beyond the scope of this study.

Figure 9 shows the same data as shown in Figure 8A but is graphed in $\ln(D^3)$ vs inverse temperature as an Arrhenius plot

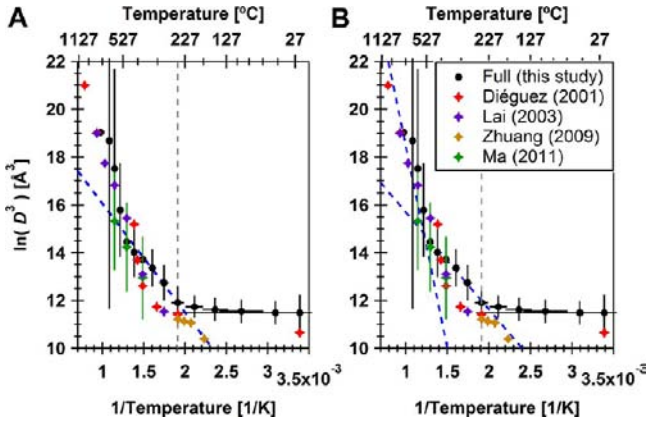

Figure 9. Arrhenius plot of SnO_2 nanoparticle growth upon elimination of sorbed water species. Data points are the same data as shown in Figure 8A. (A) Fit with a single regression line. (B) Fit with two regression lines, separating at 500 °C.

(D = particle diameter). The slope extracted from a linear fit yields the activation energy for SnO_2 grain growth. Two questions arise in regards to the growth mechanisms: One is the choice of grain growth exponent (n), and another is whether or not the growth mechanism changes as a function of temperature. It appears that even for the same nanocrystalline materials, the exponent index n used in the growth kinetic equation varies over a wide range from 2 to >4 depending on the microstructures and the growth mechanisms.[28] In Figure 9, we have arbitrarily assumed n = 3 so that the growth rate is proportional to the particle volume. As seen in Figure 9, first, nanoparticles started to grow significantly >250 °C, and upon further heating to 500 °C, the particle volume seems to increase at a much faster rate than observed below 500 °C. This indicates that different SnO_2 growth mechanisms may occur when moving from low to high temperatures. Unfortunately, the uncertainty of refined particle sizes is increased for grown SnO_2 nanocrystals due to the experimental Q-resolution (based on the Q_{damp} value, the upper limit is ~200 Å to reveal a reliable particle size). We are unable to determine whether the growth rate increased at high temperatures or remained unchanged. Therefore, two different fits were applied. Figure 9A shows a single regression fit using all the data points (weighted by errors) ≥ 250 °C, whereas Figure 9B shows a result fitted with two regression lines, separating at 500 °C data point. The activation energy (E_a) determined from the slope of these fits is given in Table 2 for n = 3−5.

E_a values shown in Table 2 are comparable to other growth studies on SnO_2 nanoparticles under various conditions, including isothermal annealing of dry powders[28] and coarsening in colloidal suspensions at room temperature[29] or during hydrothermal treatments.[30−32] Low activation energy of 32−50 kJ/mol is a common feature regardless of the growth conditions. Lai et al.[28] attributed such low activation energies (32−44 kJ/mol) to the rearrangement of atoms (e.g., Sn−O bond lengths and O−Sn−O bond angles) at the interface between the grain boundaries. The so-called orientated

dx.doi.org/10.1021/ja312030e | J. Am. Chem. Soc. 2013, 135, 6885−6895

Table 2. Activation Energy (E_a, kJ/mol) for SnO_2 Nanoparticle Growth[a]

growth exponent index n	3	4	5
Fit with One Regression Line			
all points ≥250 °C	37(8)	49(9)	62(13)
Fit with Two Regression Lines			
points between 250 and 500 °C	33(6)	44(8)	55(11)
points ≥500 °C	137(41)	183(54)	229(67)

[a]The esd values are in parentheses.

attachment (OA) growth kinetics were later observed for SnO_2 coarsened in colloidal[29] and hydrothermal[30,31] conditions. The OA growth of SnO_2 has E_a of 49.7 ± 4.8 kJ/mol[31] and occurs when two or more primary nanocrystals assumed the same orientation, yielding a larger one with twins, stacking faults and dislocation defects.[29−31,52] The OA mechanism is fundamentally similar to Lai's et al.[28] observation in the sense that both effectively reflect a reduction of overall surface area and energy of the system by eliminating the surfaces/interfaces at which the crystallites join. Accordingly, when n = 3−5, the estimated E_a values (either fitted with one or two regression lines) are small and agree with the above energies, appropriate for the rearrangement of atoms at interfaces. Other examples for small E_a are OA growth of ZnS in the hydrothermal NaOH solution (54.5 ± 5.2 kJ/mol)[53] and isothermal calcination of anatase−TiO_2 (32 ± 2 kJ/mol; n = 2).[49] The effects of Na^+/OH^- ions sorbed on ZnS[53] are considered as steric agents enhancing the OA growth, whereas the presence of hydration layers on anatase−TiO_2 is explained to be an effective passage[49] responsible for jointing adjacent nanoparticles and stimulating growth (with low E_a). Similar effects of additives and steric agents for hydrothermal OA growth of anatase−TiO_2 in deionized water are discussed by Penn and Banfield,[54] where they pointed out that water molecules can play a role of enhancing the OA phenomena. They[54,55] further suggested that OA could be important in nominally dry aggregates where particles have abundant surface-bound water, but where there is no free-flowing water. Considering that the neutron dehydration experiments were performed with hydrated nanopowders loaded in the vanadium can, it is likely that the growth behavior determined from PDF analysis is controlled by interfacial reactions. The presence of hydration water layers (and Cl contaminants on the surface) can facilitate the creation of hydrogen bonds which in turn bridges the adjacent nanoparticles, yielding the "OA-like" growth upon elimination of sorbed species. This proposed mechanism may largely depend on the sample packing density, degree of aggregation, and probability of achieving appropriate orientations within random aggregates. At higher temperatures (≥500 °C), different growth mechanisms may prevail, such as the classical Ostwald ripening[29,31,56] or the aggregation-induced fast growth as mentioned by Zhuang et al.[32] These two later processes require enough thermal fluctuations to initiate diffusion of Sn/O ions along the particle boundary or to enhance aggregations by Brownian motion of particles. For further analysis of the "OA-like" growth during isothermal annealing of hydrated nanopowders and effects of hydration level on the growth response, a combined investigation by HRTEM, PDF, and kinetic model is needed.

CONCLUSIONS

PDF analysis applied to neutron total scattering data provides structural information of sorbed water species and their role in stabilization and growth of SnO_2 nanocrystals. Although the PDF observations cannot provide unambiguous evidence about the dissociation of first-layer water on SnO_2 surfaces (due mainly to broad distribution of D−D distances and Fourier termination ripples), the hydroxylated (dissociative) MD model, along with the assumption that the nanoparticle surfaces all behave like the simulated (110) surfaces, does give a better fitted PDF fits. The a lattice contraction and its nonlinear thermal expansion upon elimination of sorbed species indicate that SnO_2 nanocrystals readily adopt minimum-energy structural configurations upon changes in the surrounding environment. Furthermore, sorbed water species and likely dominant presence of hydroxyls on SnO_2 surfaces may act like steric agents promoting nanocrystal growth during thermal dehydration. This mechanism may also occur in nature and/or during nanoparticle synthesis on a controlled substrate. Results of PGAA and TG analyses integrated with PDF and MD modeling provide strong evidence that a careful determination of surface water contents and an unambiguous structural description for surface hydration layers are critical for justification and understanding of many characteristics of hydrated nanomaterials.

ASSOCIATED CONTENT

Supporting Information

HRTEM images of as-synthesized SnO_2 nanoparticles and postexperiment grown SnO_2 crystals; preparation of SnO_2 nanocrystals with three different surface water coverages; detailed comparisons between PGAA and PDF analyses; tabulated reports of SnO_2 neutron and synchrotron X-ray PDF and Rietveld refinements; and temperature-resolved neutron total scattering S(Q) figure are provided in the Supporting Information. This material is available free of charge via the Internet at http://pubs.acs.org.

AUTHOR INFORMATION

Corresponding Author

wangh3@ornl.gov

Notes

The authors declare no competing financial interest.

ACKNOWLEDGMENTS

This research is primarily sponsored by the U.S. Department of Energy (DOE), Office of Basic Energy Sciences (BES), Division of Chemical Sciences, Geosciences and Biosciences. The research at ORNL/SNS was supported by the Scientific User Facilitates Division, BES, DOE. The support of the NIST/NCNR, U.S. Department of Commerce in providing the research neutron facility for PGAA is also acknowledged. Use of the Advanced Photon Source (APS) at Argonne National Laboratory (ANL) was supported by the DOE, BES, under contract no. DE-AC02-06CH11357. Technical assistance from Matthew R. Suchomel (11-BM beamline scientist at the ANL/APS) is gratefully acknowledged. Certain commercial equipment, instruments, materials and software are identified in this paper to foster understanding. Such identification does not imply recommendation or endorsement by the ORNL, NIST, ANL, or DOE nor does it imply that the materials or

equipment identified are necessarily the best available for the purpose.

REFERENCES

(1) Barsan, N.; Weimar, U. *J. Electroceram.* **2001**, *7*, 143.
(2) Lantto, V.; Rantala, T. T.; Rantala, T. S. *J. Eur. Ceram. Soc.* **2001**, *21*, 1961.
(3) Batzill, M.; Diebold, U. *Prog. Surf. Sci.* **2005**, *79*, 47.
(4) Chen, Z. W.; Jiao, Z.; Wu, M. H.; Shek, C. H.; Wu, C. M. L.; Lai, J. K. L. *Prog. Mater. Sci.* **2011**, *56*, 901.
(5) Edelman, F.; Hahn, H.; Seifried, S.; Alof, C.; Hoche, H.; Balogh, A.; Werner, P.; Zakrzewska, K.; Radecks, M.; Pasierb, P.; Chack, A.; Mikhelashvili, V.; Eisenstein, G. *Mater. Sci. Eng., B* **2000**, *69*, 386.
(6) Boyle, J. F.; Jones, K. A. *J. Electron. Mater.* **1977**, *6*, 717.
(7) Gercher, V. A.; Cox, D. F. *Surf. Sci.* **1995**, *322*, 177.
(8) Baraton, M.-I.; Merhari, L. *Mater. Trans.* **2001**, *42*, 1616.
(9) Batzill, M.; Katsiev, K.; Burst, J. M.; Diebold, U. *Phys. Rev. B: Condes. Matter Mater. Phys.* **2005**, *72*, 165414.
(10) Batzill, M.; Bergermayer, W.; Tanaka, I.; Diebold, U. *Surf. Sci.* **2006**, *600*, 29.
(11) Vlcek, L.; Zhang, Z.; Machesky, M. L.; Fenter, P.; Rosenqvist, J.; Wesolowski, D. J.; Anovitz, L. M.; Predota, M.; Cummings, P. T. *Langmuir* **2007**, *23*, 4925.
(12) Bandura, A. V.; Kubicki, J. D.; Sofo, J. O. *J. Phys. Chem. B* **2008**, *112*, 11616.
(13) Ma, Y.; Castro, R. H. R.; Zhou, W.; Navrotsky, A. *J. Mater. Res.* **2011**, *26*, 848.
(14) Lindan, P. J. D.; Harrison, N. M.; Gillan, M. J. *Phys. Rev. Lett.* **1998**, *80*, 762.
(15) Lindan, P. J. D. *Chem. Phys. Lett.* **2000**, *328*, 325.
(16) Bates, S. P. *Surf. Sci.* **2002**, *512*, 29.
(17) Kumar, N.; Kent, P. R. C.; Bandura, A. V.; Kubicki, J. D.; Wesolowski, D. J.; Cole, D. R.; Sofo, J. O. *J. Chem. Phys.* **2011**, *134*, 044706.
(18) Mamontov, E.; Vlcek, L.; Wesolowski, D. J.; Cummings, P. T.; Wang, W.; Anovitz, L. M.; Rosenqvist, J.; Brown, C. M.; Sakai, V. G. *J. Phys. Chem. C* **2007**, *111*, 4328.
(19) Egashira, M.; Nakashima, M.; Kawasumi, S.; Seiyama, T. *J. Phys. Chem.* **1981**, *85*, 4125.
(20) Shi, Q.; Boerio-Goates, J.; Woodfield, K.; Rytting, M.; Pulsipher, K.; Spencer, E. C.; Ross, N. L.; Navrotsky, A.; Woodfield, B. F. *J. Phys. Chem. C* **2012**, *116*, 3910.
(21) Ross, N. L.; Spencer, E. C.; Levchenko, A. A.; Kolesnikov, A. I.; Abernathy, D. L.; Boerio-Goates, J.; Woodfield, B. F.; Navrotsky, A.; Li, G.; Wang, W.; Wesolowski, D. J. *Mater. Res. Soc. Symp. Proc.* **2011**, 1352.
(22) Spencer, E. C.; Ross, N. L.; Parker, S. F.; Kolesnikov, A. I.; Woodfield, B. F.; Woodfield, K.; Rytting, M.; Boerio-Goates, J.; Navrotsky, A. *J. Phys. Chem. C* **2011**, *115*, 21105.
(23) Shek, C. H.; Lai, J. K. L.; Lin, G. M.; Zheng, Y. F.; Liu, W. H. *J. Phys. Chem. Solids* **1997**, *58*, 13.
(24) Jiang, J. Z.; Gerward, L.; Olsen, J. S. *Scr. Mater.* **2001**, *44*, 1983.
(25) Wang, Y.; Ma, C.; Sun, X.; Li, H. *Nanotechnology* **2002**, *13*, 565.
(26) Jensen, K. M. Ø.; Christensen, M.; Juhas, P.; Tyrsted, C.; Bøjesen, E. D.; Lock, N.; Billinge, S. J. L.; Iversen, B. B. *J. Am. Chem. Soc.* **2012**, *134*, 6785.
(27) Diéguez, A.; Romano-Rodríguez, A.; Vilà, A.; Morante, J. R. *J. Appl. Phys.* **2001**, *90*, 1550.
(28) Lai, J. K. L.; Shek, C. H.; Lin, G. M. *Scr. Mater.* **2003**, *49*, 441.
(29) Leite, E. R; Giraldi, T. R.; Pontes, F. M.; Longo, E.; Beltrán, A.; Andrés, J. *Appl. Phys. Lett.* **2003**, *83*, 1566.
(30) Lee, E. J. H.; Ribeiro, C.; Longo, E.; Leite, E. R. *J. Phys. Chem. B* **2005**, *109*, 20842.
(31) Zhuang, Z.; Zhang, J.; Huang, F.; Wang, Y.; Lin, Z. *Phys. Chem. Chem. Phys.* **2009**, *11*, 8516.
(32) Zhuang, Z.; Huang, F.; Lin, Z.; Zhang, H. *J. Am. Chem. Soc.* **2012**, *134*, 16228.
(33) Paul, R. L.; Lindstrom, R. M. *J. Radioanal. Nucl. Chem.* **2000**, *243*, 181.
(34) Anderson, D. L.; Failey, M. P.; Zoller, W. H.; Walters, W. B.; Gordon, G. E.; Lindstrom, R. M. *J. Radioanal. Chem.* **1981**, *63*, 97.
(35) Neuefeind, J.; Feygenson, M.; Carruth, J.; Hoffmann, R.; Chipley, K. K. *Nucl. Instrum. Methods Phys. Res., Sect. B* **2012**, *287*, 68.
(36) Farrow, C. L.; Juhas, P.; Liu, J. W.; Bryndin, D.; Bozin, E. S.; Bloch, J.; Proffen, T.; Billinge, S. J. L. *J. Phys.: Condens. Matter* **2007**, *19*, 335219.
(37) Page, K.; Hood, T. C.; Proffen, T.; Neder, R. B. *J. Appl. Crystallogr.* **2011**, *44*, 327.
(38) Grigera, J. R. *J. Chem. Phys.* **2001**, *114*, 8064.
(39) Shannon, R. D. *Acta Crystallogr., Sect. A* **1976**, *32*, 751.
(40) Bolzan, A. A.; Fong, C.; Kennedy, B. J.; Howard, C. J. *Acta Crystallogr., Sect. B: Struct. Sci.* **1997**, *53*, 373.
(41) Haines, J.; Léger, J. M. *Phys. Rev. B: Condens. Matter Mater. Phys.* **1997**, *55*, 11144.
(42) Shieh, S. R.; Kubo, A.; Duffy, T. S.; Prakapenka, V. B.; Shen, G. *Phys. Rev. B: Condens. Matter Mater. Phys.* **2006**, *73*, 014105.
(43) Gracia, L.; Beltrán, A.; Andrés, J. *J. Phys. Chem. B* **2007**, *111*, 6479.
(44) Peercy, P. S.; Morosin, B. *Phys. Rev. B: Condens. Matter Mater. Phys.* **1973**, *7*, 2779.
(45) Gladysz, G. M.; Schmücker, M.; Schneider, H.; Chawla, K. K.; Joslin, D. L.; Ferber, M. K. *J. Mater. Sci.* **1999**, *34*, 4351.
(46) Ono, S.; Ito, E.; Katsura, T.; Yoneda, A.; Walter, M. J.; Urakawa, S.; Utsumi, W.; Funakoshi, K. *Phys. Chem. Minerals* **2000**, *27*, 618.
(47) Cimino, A.; Porta, P.; Valigi, M. *J. Am. Chem. Soc.* **1966**, *49*, 152.
(48) Tsunekawa, S.; Ishikawa, K.; Li, Z. Q.; Kawazoe, Y.; Kasuya, A. *Phys. Rev. Lett.* **2000**, *85*, 3440.
(49) Li, G.; Boerio-Goates, J.; Woodfield, B. F.; Li, L. *Appl. Phys. Lett.* **2004**, *85*, 2059.
(50) Dai, Z. R.; Gole, J. L.; Stout, J. D.; Wang, Z. L. *J. Phys. Chem. B* **2002**, *106*, 1274.
(51) Arbiol, J.; Comini, E.; Faglia, G.; Sberveglieri, G.; Morante, J. R. *J. Cryst. Growth* **2008**, *310*, 253.
(52) Penn, R. L.; Banfield, J. F. *Am. Mineral.* **1998**, *83*, 1077.
(53) Zhang, J.; Lin, Z.; Lan, Y.; Ren, G.; Chen, D.; Huang, F.; Hong, M. *J. Am. Chem. Soc.* **2006**, *128*, 12981.
(54) Penn, R. L.; Banfield, J. F. *Geochim. Cosmochim. Acta* **1999**, *63*, 1549.
(55) Penn, R. L.; Banfield, J. F. *Science* **1998**, *281*, 969.
(56) Lifshift, I. M.; Slyozov, V. V. *J. Phys. Chem. Solids* **1961**, *19*, 35.